The Astrophysical Journal Letters, 949:L31 (14pp), 2023 June 1 https://doi.org/10.3847/2041-8213/acd54b

The Population of the Galactic Center Filaments: Position Angle Distribution Reveals a Degree-scale Collimated Outflow from Sgr A* along the Galactic Plane

F. Yusef-Zadeh[1], R. G. Arendt[2,3], M. Wardle[4], and I. Heywood[5,6]
[1] Dept Physics and Astronomy, CIERA, Northwestern University, 2145 Sheridan Road, Evanston, IL 60207, USA; zadeh@northwestern.edu
[2] Code 665, NASA/GSFC, 8800 Greenbelt Road, Greenbelt, MD 20771, USA; Richard.G.Arendt@nasa.gov
[3] 2NASA/GSFC, Code 665, 8800 Greenbelt Road, Greenbelt, UMBC/CRESST 2, MD 20771, USA
[4] Research Centre for Astronomy, Astrophysics and Astrophotonics, Macquarie University, Sydney NSW 2109, Australia; mark.wardle@mq.edu.au
[5] Astrophysics, Department of Physics, University of Oxford, Keble Road, Oxford, OX1 3RH, UK; ian.heywood@physics.ox.ac.uk
[6] Department of Physics and Electronics, Rhodes University, PO Box 94, Makhanda, 6140, South Africa
Received 2023 April 17; revised 2023 May 5; accepted 2023 May 9; published 2023 June 2

Abstract

We have examined the distribution of the position angle (PA) of the Galactic center filaments with lengths $L > 66''$ and $<66''$ as well as their length distribution as a function of PA. We find bimodal PA distributions of the filaments, and long and short populations of radio filaments. Our PA study shows the evidence for a distinct population of short filaments with PA close to the Galactic plane. Mainly thermal, short-radio filaments ($<66''$) have PAs concentrated close to the Galactic plane within $60° < \mathrm{PA} < 120°$. Remarkably, the short filament PAs are radial with respect to the Galactic center at $l < 0°$ and extend in the direction toward Sgr A*. On a smaller scale, the prominent Sgr E H II complex G358.7-0.0 provides a vivid example of the nearly radial distribution of short filaments. The bimodal PA distribution suggests a different origin for two distinct filament populations. We argue that the alignment of the short-filament population results from the ram pressure of a degree-scale outflow from Sgr A* that exceeds the internal filament pressure, and aligns them along the Galactic plane. The ram pressure is estimated to be 2×10^6 cm^{-3} K at a distance of 300 pc, requiring biconical mass outflow rate $10^{-4}\,M_\odot$ yr^{-1} with an opening angle of $\sim$40°. This outflow aligns not only the magnetized filaments along the Galactic plane but also accelerates thermal material associated with embedded or partially embedded clouds. This places an estimate of $\sim$6 Myr as the age of the outflow.

Unified Astronomy Thesaurus concepts: Galactic center (565); Interstellar Filaments (842); Non-thermal radiation Soucrces (1119)

1. Introduction

The prototype magnetized radio filaments in the Galactic center (GC) were discovered close to 40 years ago (Yusef-Zadeh et al. 1984). Since then, Very Large Array (VLA), Nobeyama 45m-telescope, Mologlo, and ATCA observations have shown linearly polarized synchrotron emission tracing nucleus-wide cosmic-ray activity throughout the inner few hundred parsecs of the Galaxy (Liszt 1985; Bally & Yusef-Zadeh 1989; Gray et al. 1991; Sofue et al. 1992; Lang et al. 1999; Reich et al. 2000; Nord et al. 2004; Yusef-Zadeh et al. 2004; LaRosa et al. 2005; Law et al. 2008; Pound & Yusef-Zadeh 2018; Arendt et al. 2019; Staguhn et al. 2019). Chandra, XMM-Newton (XMM), and NuSTAR have also detected X-ray emission from a handful of nonthermal radio filaments. (Lu et al. 2003; Sakano et al. 2003; Yusef-Zadeh et al. 2005; Zhang et al. 2014, 2020; Yusef-Zadeh et al. 2021).

High-temperature molecular clouds with large, turbulent line widths also characterize this region, the Central Molecular Zone (CMZ). Furthermore, H_3^+ absorption line observations show that high cosmic-ray ionization rates permeate the CMZ at levels 1000 times that of the solar neighborhood (Oka & Geballe 2020). These observations indicate that cosmic-ray pressure in the CMZ is significant when compared to the interstellar gas pressure of the GC.

Recent MeerKAT observations have provided a remarkable mosaic of the inner few degrees of the GC with exquisite details at 4″–6″ spatial resolution (Heywood et al. 2019, 2022). Statistical properties of the population of GC filaments such as morphology, mean spectral index, equipartition magnetic field, filament spacing and filament association with stellar candidates have recently been studied in detail in a series of papers (Yusef-Zadeh et al. 2022a, 2022b, 2022c). VLA observations showed the bright and long filaments emitting nonthermal emission, whereas MeerKAT data showed a great deal of fainter filaments and filamentary structures that are shorter. MeerKAT has also surveyed a large number of galaxy clusters, some of which show exceptional isolated filamentary structures in the intracluster medium (ICM). These filaments appear to be linked to radio jets, tails, and lobes of radio galaxies (Shimwell et al. 2016; Ramatsoku et al. 2020; Condon et al. 2021; Rudnick et al. 2022). For the first time, a population of magnetized ICM filaments, with an underlying physical mechanism similar to that of the GC filament population, is identified in external galaxies (Yusef-Zadeh et al. 2022d).

With the new and sensitive MeerKAT images of the Galactic center (GC), we continue examining the physical properties of the GC filaments, focusing on their position angle (PA). This physical characteristic could potentially provide additional insight into the origin of the enigmatic GC filaments. Previous VLA observations of the brightest GC filaments showed that they are mainly oriented perpendicular to the Galactic plane (Yusef-Zadeh et al. 2004 and references therein). Using the high sensitivity of MeerKAT data, we examine statistical properties of the PA of the GC filament population. We present evidence that short filaments located on the negative Galactic longitudes have PAs that run mainly within ±20° of the

Galactic plane. An extension of the filament PAs show radial distribution, pointing in the direction toward Sgr A* at the GC. The orientation of a large number of filaments within a few hundred parsecs of Sgr A* is similar to those found in radio continuum and recombination line images of the inner few arcminutes of Sgr A* (Royster et al. 2019; Yusef-Zadeh et al. 2020). In addition, ALMA observations of the Sgr E molecular cloud shows parallel filamentary structure along the Galactic plane (Wallace et al. 2022). Here we consider a picture in which a collimated outflow, most likely arising from Sgr A*, is responsible for distorting and aligning the shape of molecular, thermal, and nonthermal features along the Galactic plane.

2. Data Reduction

Details of the MeerKAT observations can be found in Heywood et al. (2022). Here we briefly describe the observations and data processing. The final image is constructed from 20 MeerKAT pointings for a total of 144 hr on source. The *L*-band (856–1712 MHz) system was used, with the correlator configured to deliver 4096 frequency channels. The 1.28 GHz mosaic covers the inner $\sim 3^\circ.5 \times \sim 2^\circ.5$ ($l \times b$) of the GC. Spectral index (α) measurements (where $I_\nu \propto \nu^\alpha$)) have used 16 sub-bands between 856 and 1712 MHz. The in-band spectral index values are measured simultaneously, centered at 1.28 GHz (Heywood et al. 2022).

To enhance the visibility of the filaments, the mosaic image is filtered using a difference of Gaussians to smooth noise and remove large-scale backgrounds, as described in detail in Yusef-Zadeh et al. (2022a). Numerous fainter filaments are uncovered and stand out in the filtered image. To confirm the reality of faint filaments in the filtered image, we have found their counterparts in the unfiltered image. There are a large number of twisted short features associated with H II regions and nonthermal filaments. Our analysis includes the long and short filaments, both of which consist of a mixture of thermal and nonthermal features. The lengths (*L*) and mean PAs of the filaments are measured by application of the procedure *LOOPTRACING_AUTO* (Aschwanden 2010). A detailed account of this procedure will be given elsewhere.

3. Results

The 4″ resolution MeerKAT image of the GC is shown in Figure 1 (top panel). A filtered image of the same mosaic image is shown in Figure 1 (bottom panel) with a resolution of ∼6.″4. supernova remnants (SNRs) and foreground H II complexes are drawn with red circles on Figure1 (top and bottom panels). Our analysis excludes these features that would otherwise contaminate our analysis of individual filaments in the GC.

3.1. Filament Length as Function of the PA

Figure 2 shows three different representations of color-coded identified filaments with different PA ranges with respect to Galactic north (PA = 0°), traced by different color tables. Figure 2(a) shows the full range of filament PAs between 0° and 180° (or equivalently, −90° to +90°) with different colors. Color tables are used in order to distinguish between the filaments with positive (red) and negative (blue) PAs. The distribution suggests that the filaments oriented perpendicular to the Galactic plane tend to be long. On the other hand, filaments with PAs running parallel to the Galactic plane are short. Figure 2(b) shows the distribution of short filaments, with PAs being preferred along the Galactic plane $60^\circ < \mathrm{PA} < 120^\circ$. This distribution is more obvious at negative longitudes where short filaments with PA ∼ 120° appear blue and point toward the GC. Figure 2 (bottom panel) displays the filaments with $-60^\circ < \mathrm{PA} < 60^\circ$, indicating that vertical filaments are dominated by long filaments at positive and negative latitudes. An extension of the long filaments toward the Galactic plane do not converge toward a single origin such as Sgr A* but to the inner degree of the GC.

3.2. Long Filaments PAs

Another way to characterize the distribution of filament PAs is by restricting their lengths rather than their PAs, as was described above. There is generally a continuum of filament lengths, and 66″ was chosen as a lower limit that eliminated most filaments associated with known thermal sources such as H II regions. An even cleaner selection at 132″ was discussed, but the sample size starts to become small (Yusef-Zadeh et al. 2022a). This convenient division was selected using 60 pixels with a pixel size of 1.″1 in the original MeerKAT image with a resolution of 4″ (Yusef-Zadeh et al. 2022a).

Figure 3 (top panel) shows a histogram of long filaments with $L > 66''$ as a function of PA, emphasizing long nonthermal filaments, and largely excluding thermal features. A Gaussian fit to this histogram peaks at −3.°2 with 1σ error of 12.°9. Figure 3 (bottom panel) shows a histogram of long filaments with restricted PAs ranging between −60° and 60°. We note that long filaments have a negative spectral index α, the spectral index consistent with being nonthermal. There are also a number of long filaments with $\alpha \sim -0.15$. These also are most likely associated with a network of filaments associated with the Radio Arc near $l \sim 0.2$, which are known to have a flat spectral index (Yusef-Zadeh et al. 2022a and references therein).

Another view of the PA distribution of the filaments is presented by plotting them as a function of Galactic longitude. The PA distribution of long filaments as a function of Galactic longitude is displayed in Figure 4 (top panel), whereas the same distribution only for short filaments is shown in Figure 4 (bottom panel). Each black dot represents the PA of a filament. If the filament PAs were randomly distributed, there would not be any concentration. We note a high concentration of PAs in two clusters, one near PA ∼ 20°, $l \sim 0.^\circ 2$ and the other near PA ∼ −30°, $l \sim -0.^\circ 25$. A higher concentration of filaments at $l > 0^\circ$ is due to a larger number of filaments associated with the Radio Arc near $l \sim 0.^\circ 2$. An additional concentration of short filaments is noted near $l \sim 0.^\circ 4$ with PAs along the Galactic plane, as demonstrated in Figure 4 (bottom panel).

We also note that, similar to Figure 2 (bottom pnael), the two concentrations in Figure 4 (top panel), show that the PA of the long filaments are tilted away from the Galactic north. We note that at $l < 0^\circ$, the filament PAs of the concentrations are more widely distributed than those at $l > 0^\circ$. Figure 4 (top panel) shows that within the range $0.^\circ 5 < l < -0.^\circ 75$, long filaments generally are found with $PA \sim 0^\circ$, indicating a vertical orientation. For $l > 0.^\circ 5$, the long filaments have random orientations. For $l \sim -0.^\circ 75$, long filaments are loosely clustered around PA = ±90°.

3.3. Short Filaments PA

One of the most striking aspects of our PA study of the GC filaments is the evidence for a distinct population of filaments

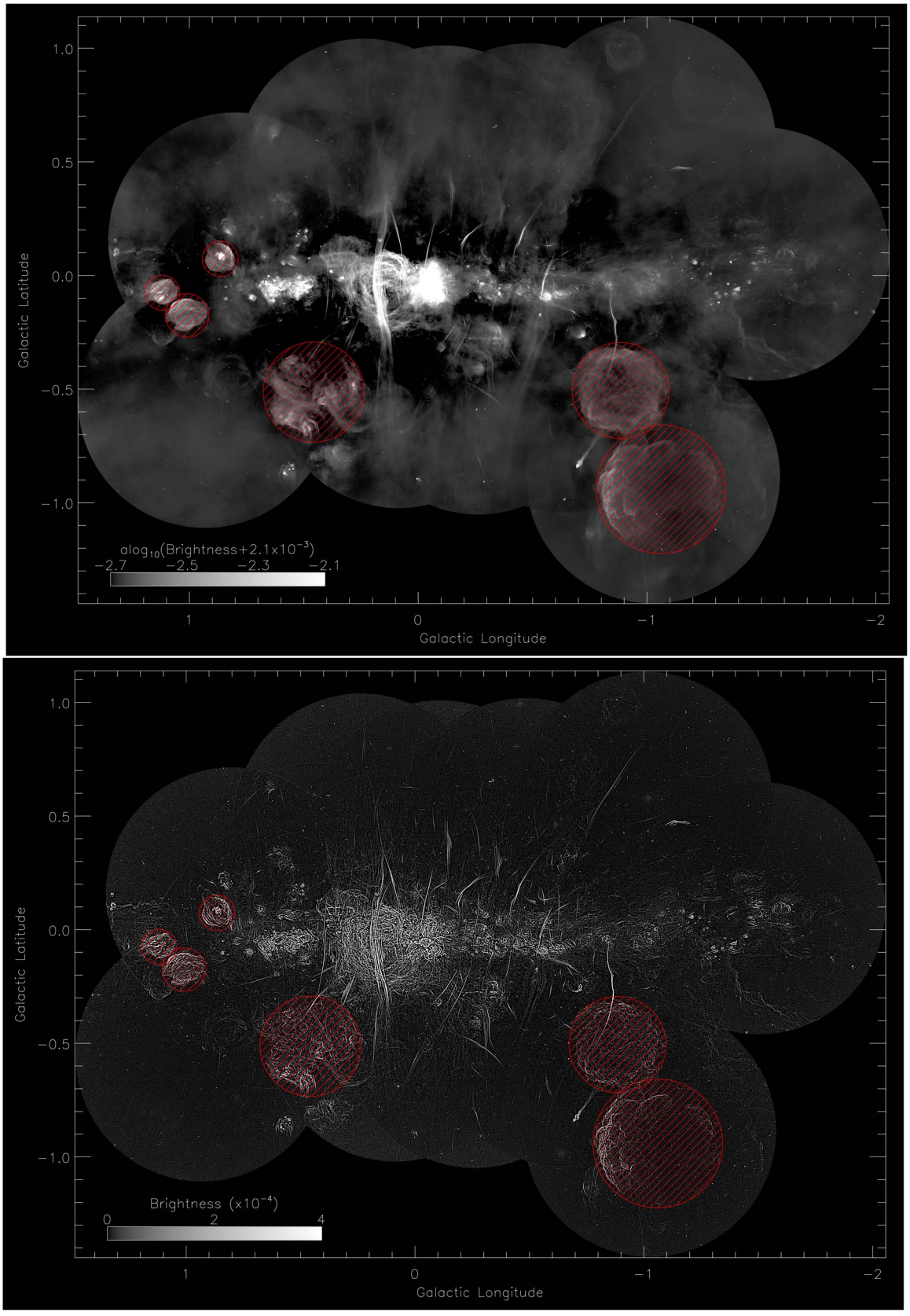

Figure 1. Top panel: a mosaic MeerKAT image of the GC at 20 cm with a 4″ resolution (Heywood et al. 2022). Bottom Panel: similar to top but filtered image with a 6.″4 resolution (Yusef-Zadeh et al. 2022a). The units are reported in Jy beam^{-1}, where the beam area is that of the original 4″ beam. The filtering process reduces the numerical value of the brightness in filament pixels by a factor of ∼0.13, with large variations due to the effect of the background removal. This factor is not applied to the filtered image intensities. Supernova remnants and H II regions identified as red circles in both top and bottom panels are excluded in the analysis.

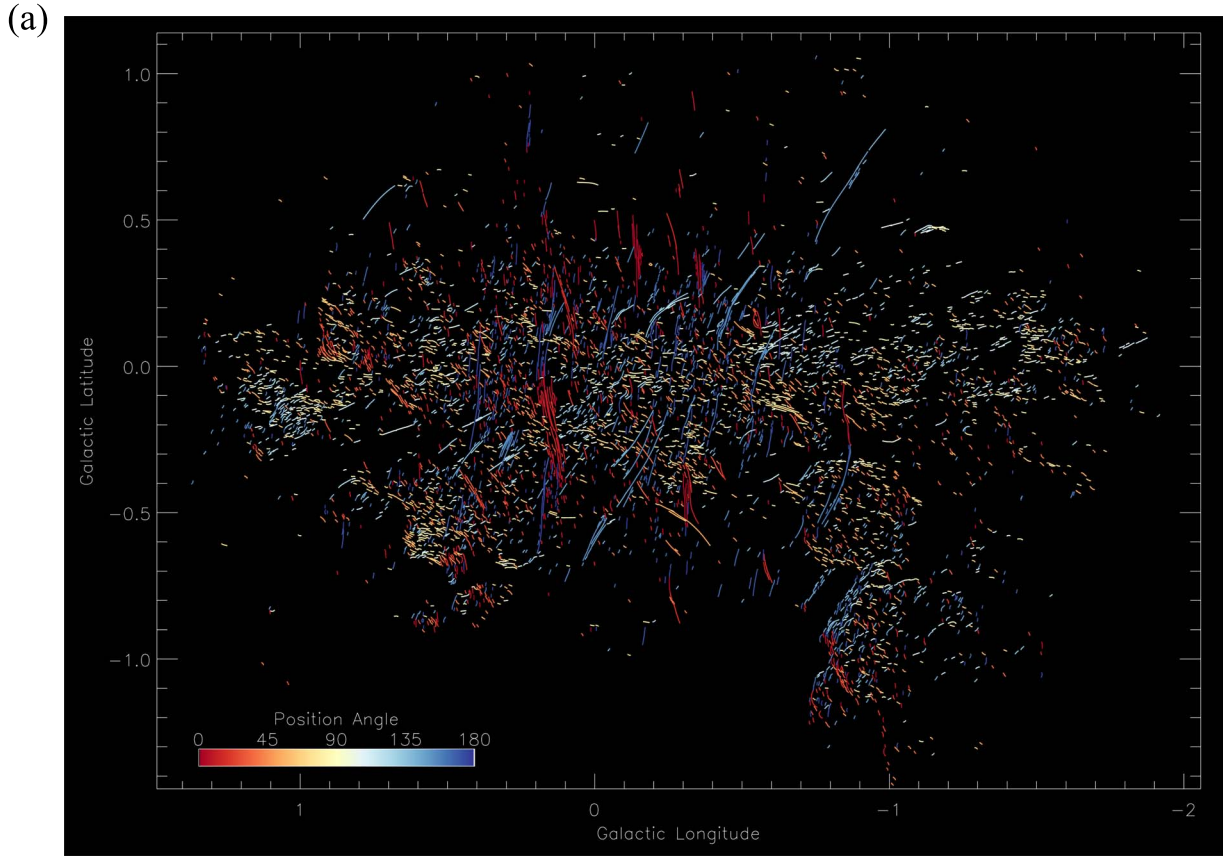

Figure 2. (a) Color-coded position angles for all identified short and long filaments in the mosaic image (Figure 1) are displayed (east of Galactic north is positive). (b) Similar to (a) except that the color table is restricted, indicating a preferred direction of short filaments $L < 66''$. The filament PAs run between 60° and 120°. Bottom panel: similar to (b) except that the color table is restricted, selecting only long filaments $L > 66''$ with PAs between −60° and 60°.

with PA close to the Galactic plane. This distribution is orthogonal to the PA distribution of long filaments that are aligned close to the Galactic north−south orientation. Figure 5 (top panel) shows the PA distribution of short ($L < 66''$) filaments. The short filament PAs are modulated by two peaks near 70° and −10°. The filaments in the peak at PAs $\sim 70°$ with a width of ∼40° are distributed mainly within $\sim\pm 20°$ of the the Galactic plane, whereas the filaments that peak close to PAs $\sim -10°$ are oriented closer to the Galactic north−south direction, having a distribution similar to that of the long filaments. In some cases the filaments can only be reliably traced over partial segments of the filament due to limited signal-to-noise and confusion.

Another characteristic that distinguishes short from long filaments is their spectral index. Figure 5 (bottom panel) shows a histogram of the spectral indices of short filaments $L < 66''$, restricted to angles within ∼30° of the Galactic plane ($60° < \mathrm{PA} < 120°$). The majority of short filaments have spectral indices consistent with thermal emission though we cannot exclude that they could be nonthermal filaments similar to the filaments of the Radio Arc near $\sim 0.^{\circ}2$. This histogram also indicates that some short filaments are nonthermal with a steep spectrum.

The distribution of PAs is also examined as a function of the Galactic PA (GPA) defined as $\arctan(l/b)$. $0° < \mathrm{GPA} < 90°$ corresponds to the NE quadrant of the GC, and subsequent 90° intervals are the SE, SW, and NW quadrants. The black points represent the PA of short- and long-identified filaments in Figures 6(a), (b), respectively. The dark diagonal line shows the expected PA distribution along a radial direction following a PA, which is equal to its GPA. Filaments along these lines are oriented radially with respect to the GC. However, we note a concentration of points close to GPA =270° (close to the Galactic plane and west of Sgr A*) along the Galactic plane. There is a tendency that filament PAs in the third GPA < 270° and fourth quadrant GPA >270° display horizontal components with PAs ∼ 70° and ∼110°, respectively. This range of filament PAs follow the diagonal line that points in the direction of Sgr A*. The width of the group of filaments following the diagonal line is about 20° above and below the Galactic plane. These trends indicate that filament PAs both north and south of the Galactic plane tend to be slightly more normal (rather the parallel) to the Galactic plane than would be expected for a purely radial distribution of filaments. Figure 6(c) schematically indicates that this trend could result from a strong radial trend (long magenta arrows). Deviations of filament PAs from the radial direction could result from the direction of orbital motion of individual sources when superimposed with radial direction of the outflow.

3.3.1. Short Filaments PA in Sgr E

A more detailed representation of the radial distribution of short filament PAs pointing toward the GC can be viewed in the spatial distribution of filaments PA in the prominent Sgr E H II complex G358.7-0.0, providing a vivid example of the nearly radial distribution of short filaments. This star-

(b)

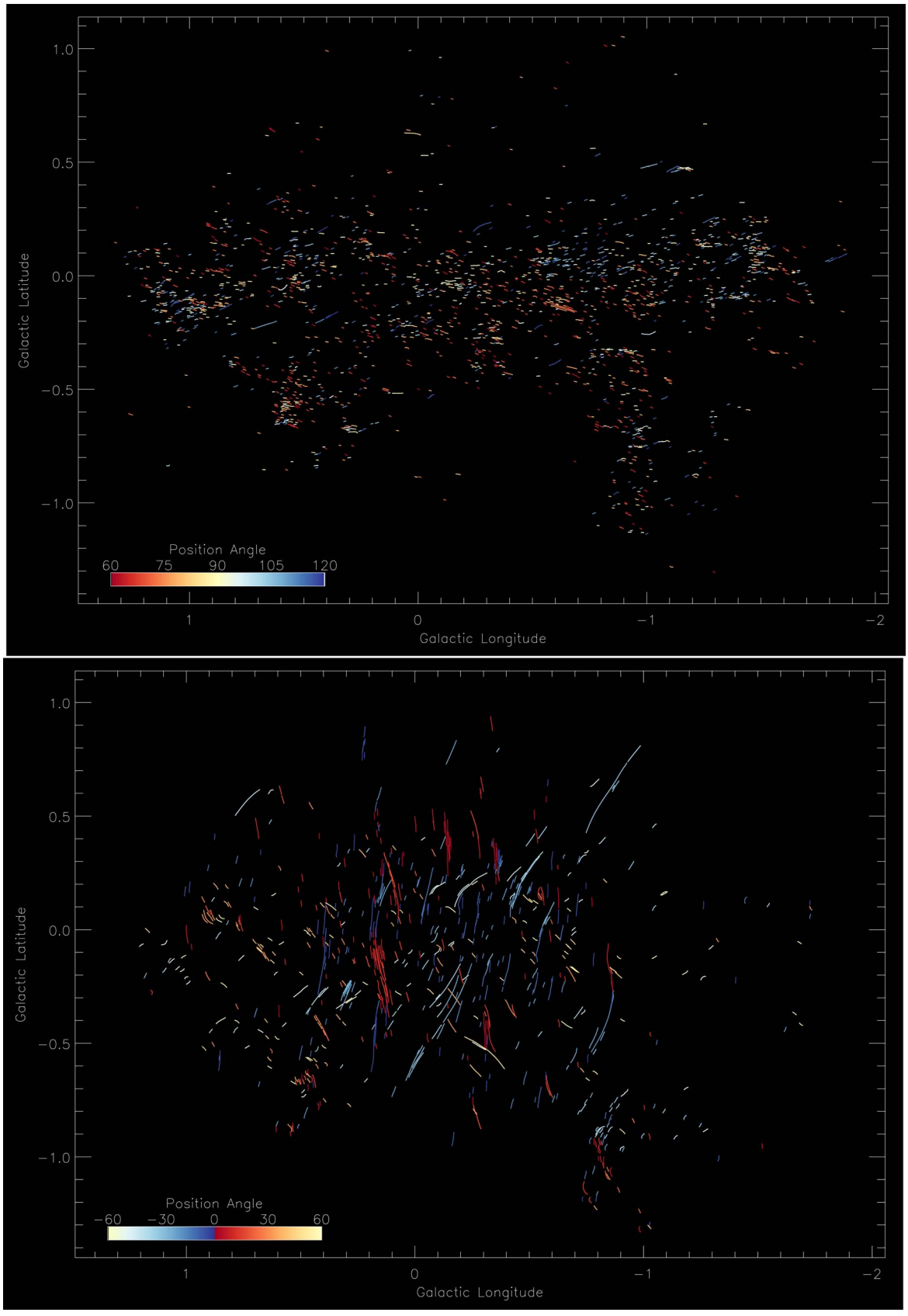

Figure 2. (Continued.)

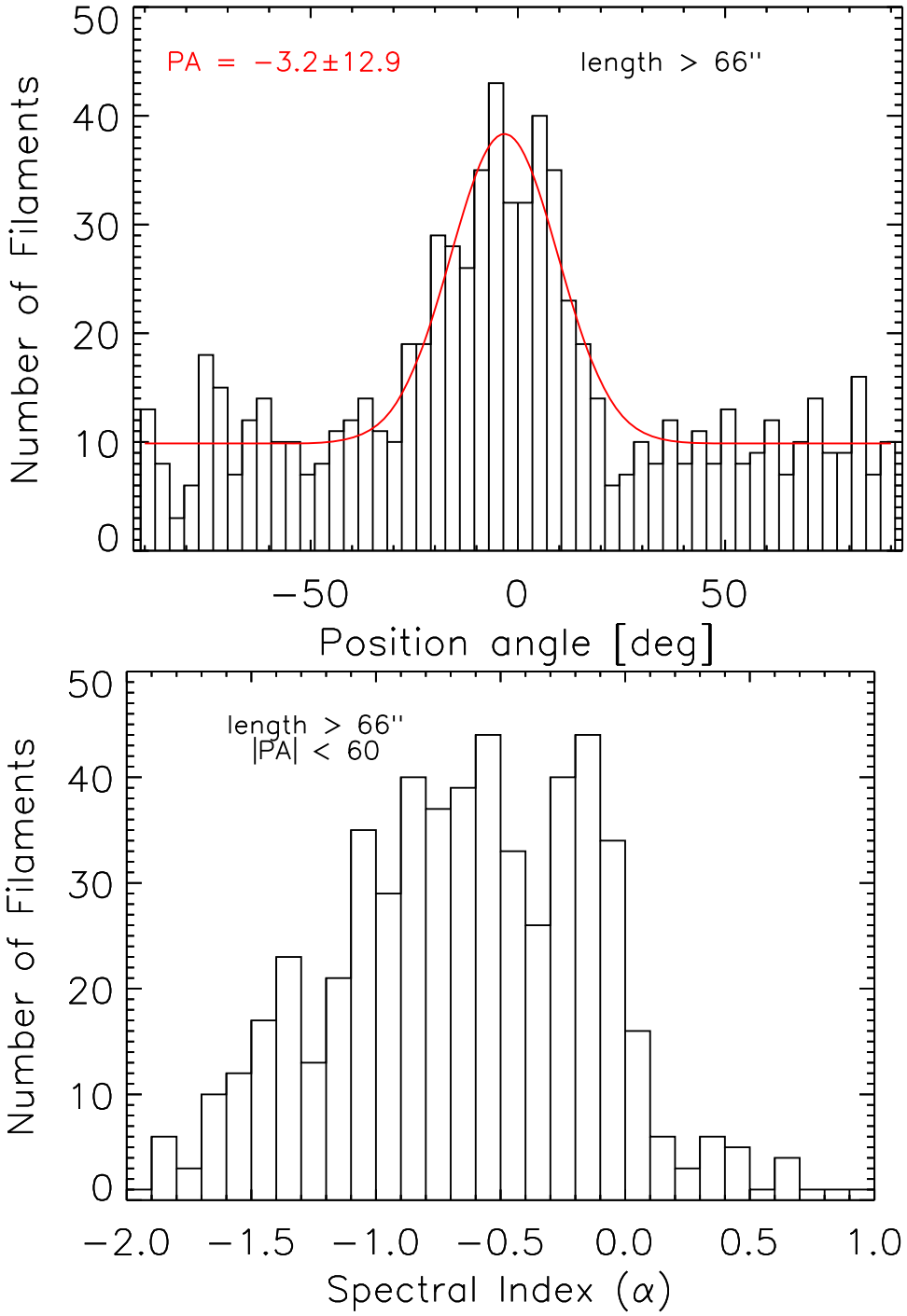

Figure 3. Top panel: a histogram of the PA distribution of filaments with lengths $L > 66''$. Galactic north has PA = 0°. Bottom panel: similar to top except for the spectral index distribution. Known SNRs and H II regions have been masked.

forming cloud contains a number of discrete H II regions that have been imaged using the VLA, Green Bank Telescope (GBT), and MeerKAT (Gray et al. 1993; Gray 1994; Cram et al. 1996; Yusef-Zadeh et al. 2004; Law et al. 2008b). Figure 7(a) displays an unfiltered 20 cm continuum MeerKAT image of the Sgr E discrete H II regions distributed around the southern half of a 0.°4 ring-shaped structure (Yusef-Zadeh et al. 2004). The northern half of Sgr E is dominated by extended diffuse emission. Some filamentary features in Sgr E appear to be correlated with structure in IR emission There is no correlation in structure between traditional nonthermal radio filaments and IR emission. This is one reason that we argued that short filaments could be thermal.

Figure 7(b) is similar to 7(a) except that a filtered image more clearly shows the large number of filamentary features. The white contour shows the outer boundary of ^{13}CO (2-1) emission from the Sgr E cloud with a mass of 3×10^5 $M_\odot$ (Anderson et al. 2020). The ^{13}CO mean velocity is −170 km s^{-1} in the SE, becoming more negative to –220 km s^{-1} toward the NW (Anderson et al. 2020). The identification of specific filaments with measured PAs is indicated by red lines in Figure 7(c).

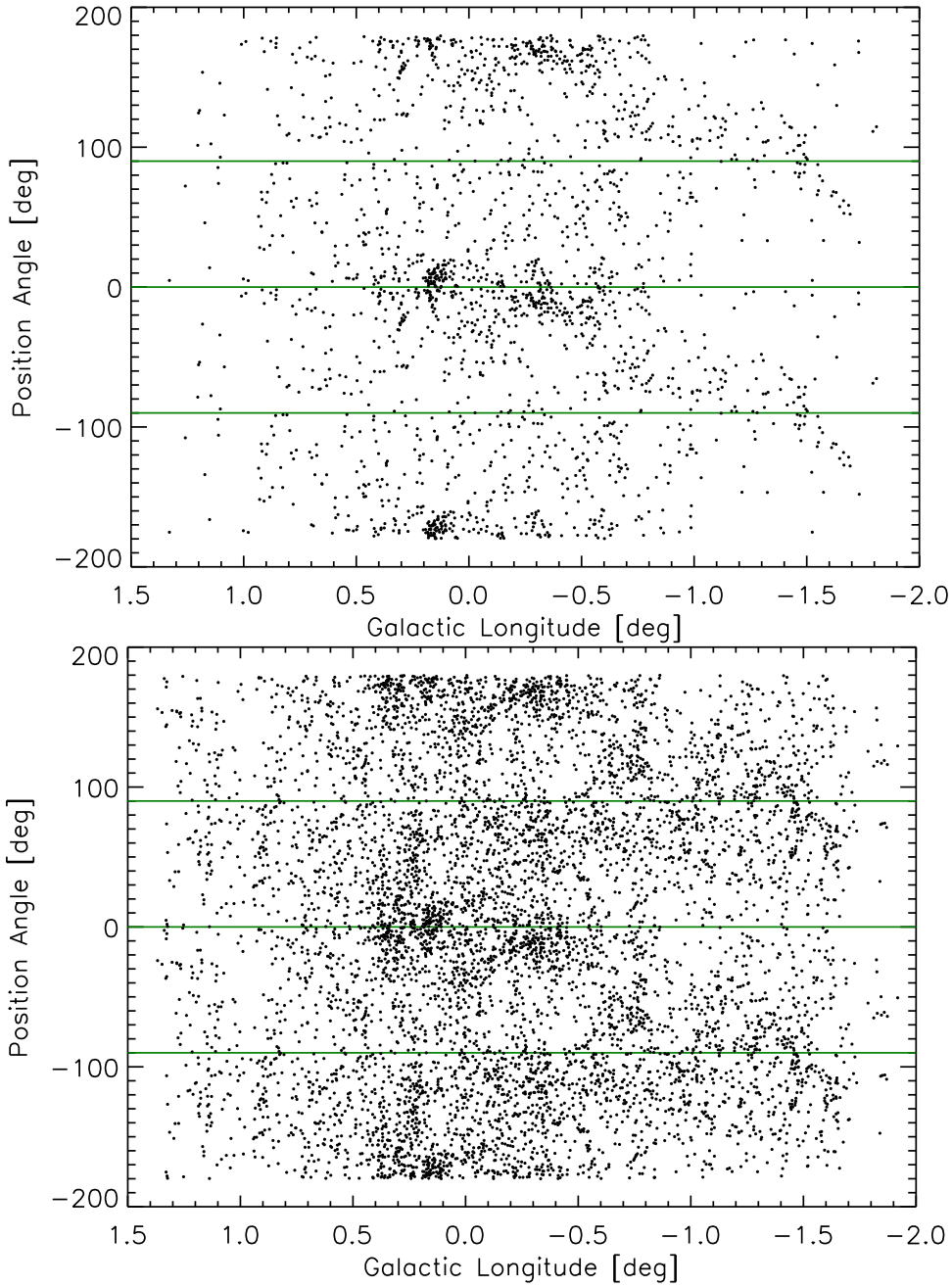

Figure 4. Top panel: the PAs of filaments with $L > 66''$, represented by a point, is shown as a function of Galactic longitude. A clustering of PAs slightly greater and slightly less than 0° are located near Galactic longitudes $l \sim 0.^{\circ}2$ and $\sim -0.^{\circ}3$, respectively. Bottom panel: similar to top except that the filament PAs are restricted to $L < 66''$. Excluded regions shown in Figure 1 are applied before top and bottom panels were constructed.

The histogram of the PAs of these filaments in Sgr E, as shown in Figure 7(d), indicates that filament PAs peak near PA $\sim 92.^{\circ}3$ within $1\sigma = 39°$, as the Gaussian fit (red) shows. The PA distribution in Sgr E is consistent with larger-scale distribution of filament PAs at negative Galactic longitudes, thus implying that the same mechanism is responsible for the origin of the filaments on this smaller, sub-degree scale.

This pattern of radial structure close to the Galactic plane is seen on even small-scale observations of some of the compact molecular clouds in the region. Recent ALMA observations of CO associated with the Sgr E complex finds two molecular filaments running close to the Galactic plane within ALMA's $52''$ field of view. These molecular filaments have an aspect ratio of ∼5 to 1 and show alignment within 2° of the Galactic plane (Wallace et al. 2022) and appear to align radially toward the GC. The origin of this filamentary structure is suggested to be due to stretching of the Sgr E cloud by the gravitational field of the Galactic bar potential. The PAs of the CO filaments resemble those found in our radio continuum study, so it is possible that they are produced by the mechanism responsible for aligning the radio filaments. MeerKAT radio image shows a short filament G358.712 + 0.027 with an extent of $\sim 1'$ and a PA of 106° (a deviation of 15° from a radial orientation), possibly associated with the molecular filament.

Figures 7(a), (b) also display a broadly triangular dark feature bounded by the lines of H II regions on the SE and SW and also the CO contours on the SW and north. The mean

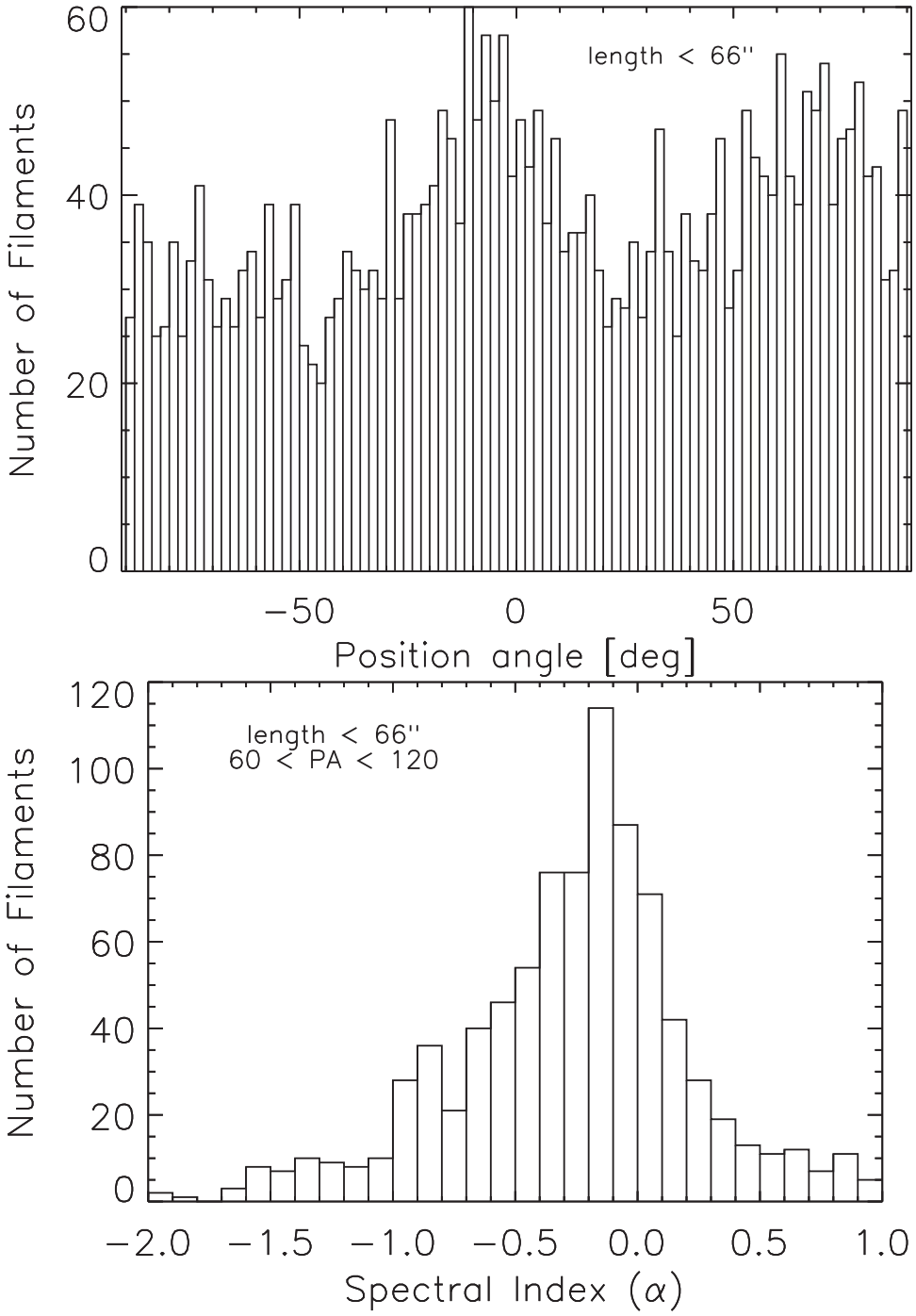

Figure 5. Top panel: similar to Figure 3 top panel, except for short filaments ($L < 66''$). Bottom panel: similar to Figure 3 bottom panel, except for short filaments ($L < 66''$).

brightness of 47 μJy beam^{-1}, corresponding to a brightness temperature of $\sim 2\overset{\circ}{.}2$ K, is coincident with contours of molecular CO in the southern half of the ring-shaped structure. To examine if this dark feature is real, we examined radio continuum image of the GC at 8 GHz observed with the GBT (Law et al. 2008b). The dark feature is clearly seen toward the Sgr E cloud, and the estimated brightness temperature toward the cloud, $\sim 9.7 \times 10^{-3}$ Jy beam^{-1}, is a factor of ~ 2 lower than the background diffuse emission. The deficit of ~ 10 mJy per $88''$ GBT beam is equivalent to an emission measure drop of $n_e^2 L_c \approx 560$ cm^{-6} pc for a line of sight through the radio dark cloud. Adopting a path length $L_c = 14$ pc through the cloud, equivalent to $0\overset{\circ}{.}1$ at 8 kpc, we find an equivalent electron density deficit $n_e \approx 6$ cm^{-3}. Making the reasonable assumption that the scale of external ionized medium has similar path length, it provides a rough estimate of the density of the external ionized medium surrounding the cloud.

The dark feature in the continuum MeerKAT and GBT images is anticorrelated with the Sgr E CO cloud. This dark feature shows similar appearance to many GC molecular clouds that have been identified as radio dark clouds (Yusef-Zadeh 2012). We interpret that the dark feature in Sgr E

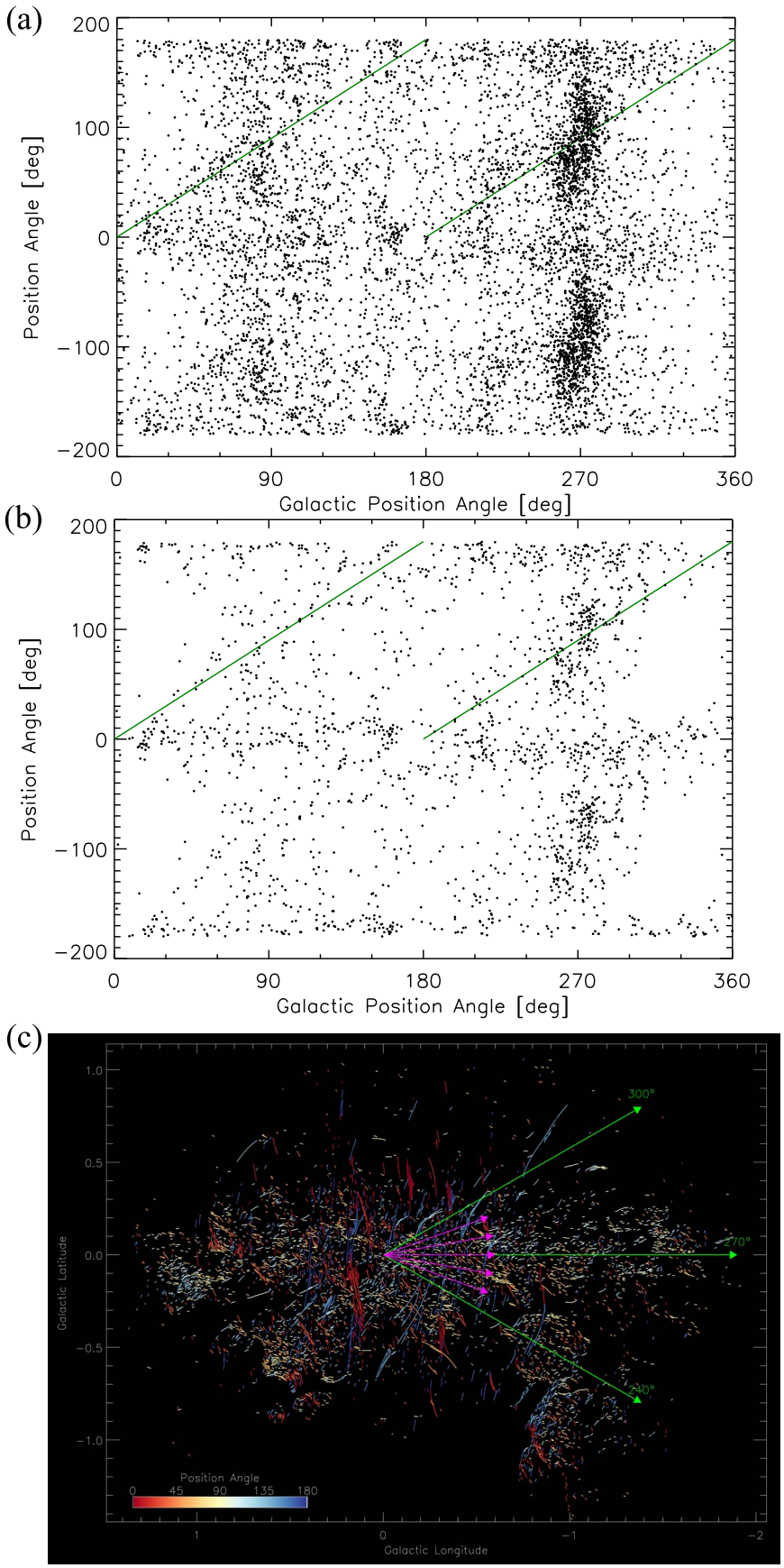

Figure 6. (a) The clump of points near GPA = 270° with GPA GPA = $tan^{-1} l/b$) < 270° identify shorter-filament PAs that are mostly below the radial trend (orange line). Those with GPA >270° (fourth quadrant) have PAs that are generally above the radial trend with steeper values, suggesting that they are close to the Galactic plane. On the other hand, at GPA <270° (third quadrant) filament PAs are generally flatter, running away from the Galactic plane. (b) The same as (a) except for long filaments. (c) A diagram showing the PAs of short filaments within a cone pointed toward the direction of Sgr A*.

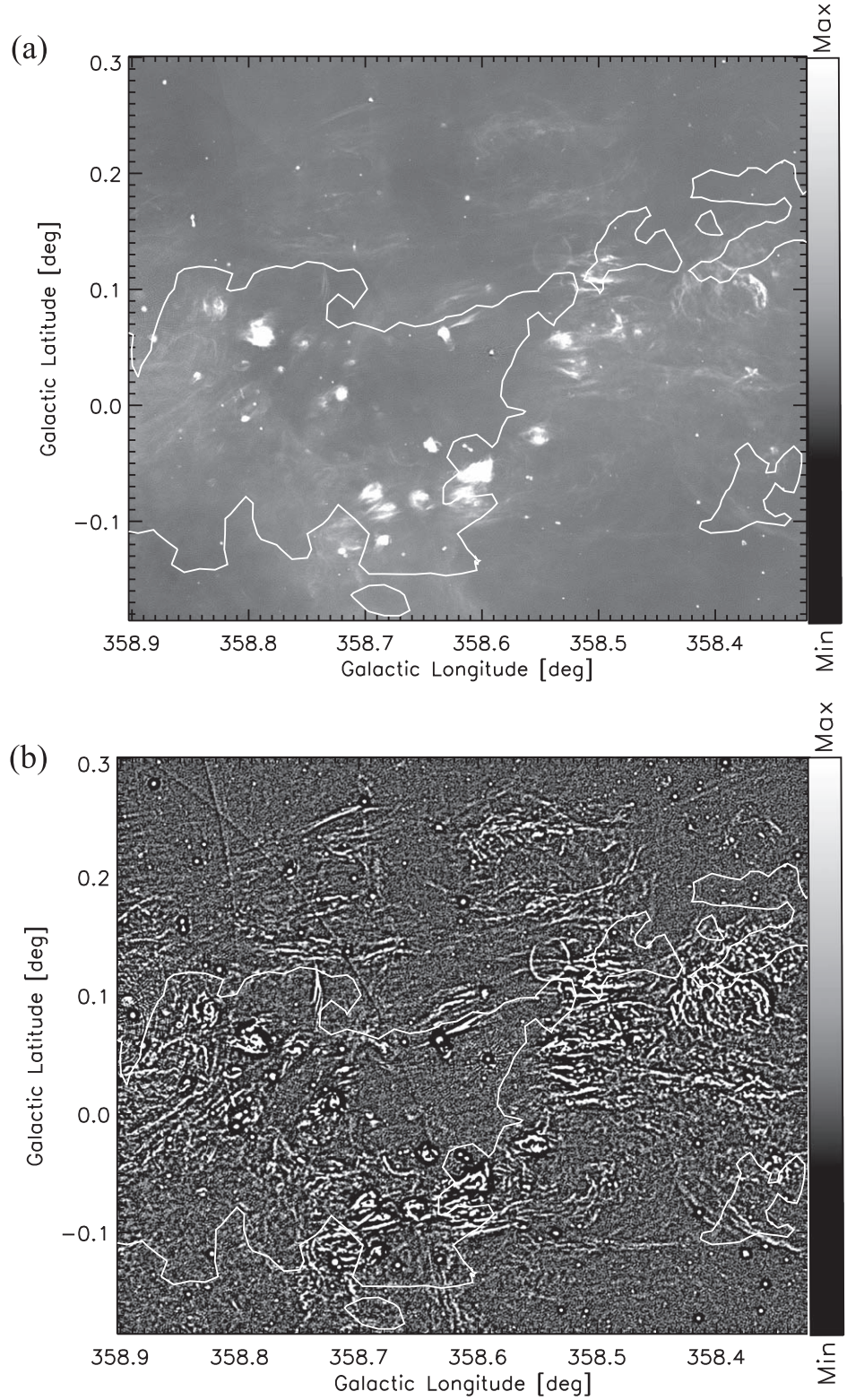

Figure 7. (a) Unfiltered continuum MeerKAT image of the Sgr E H II complex G358.7-0.0 at 20 cm showing a cluster of discrete H II regions surrounding a dark cavity coincident with the Sgr E molecular cloud (Heywood et al. 2022). The outline of ^{13}CO (2-1) line emission from the Sgr E cloud is shown as white contour (Anderson et al. 2020). The range of gray scale is [-5e-4, 7e-4] Jy beam^{-1}. (b) Similar to (a) except filtered continuum image is displayed (Yusef-Zadeh et al. 2022a). The range of gray scale is [-2e-5, 7e-5] Jy beam^{-1}. (c) Same as (b) except that identified filaments are drawn in red. The range of gray scale is [-2e-5, 7e-5] Jy beam^{-1}. (d) A histogram of filament PAs in Sgr E shows that most filaments PA are distributed within ∼40°. Red line shows a Gaussian fit to the histogram of the Galactic plane.

surrounded by compact H II regions is produced by a deficiency in radio continuum emission from molecular clouds that are embedded in a bath of UV radiation. The deficit of the continuum emission from the volume occupied by molecular gas results in dark features that trace embedded molecular clouds.

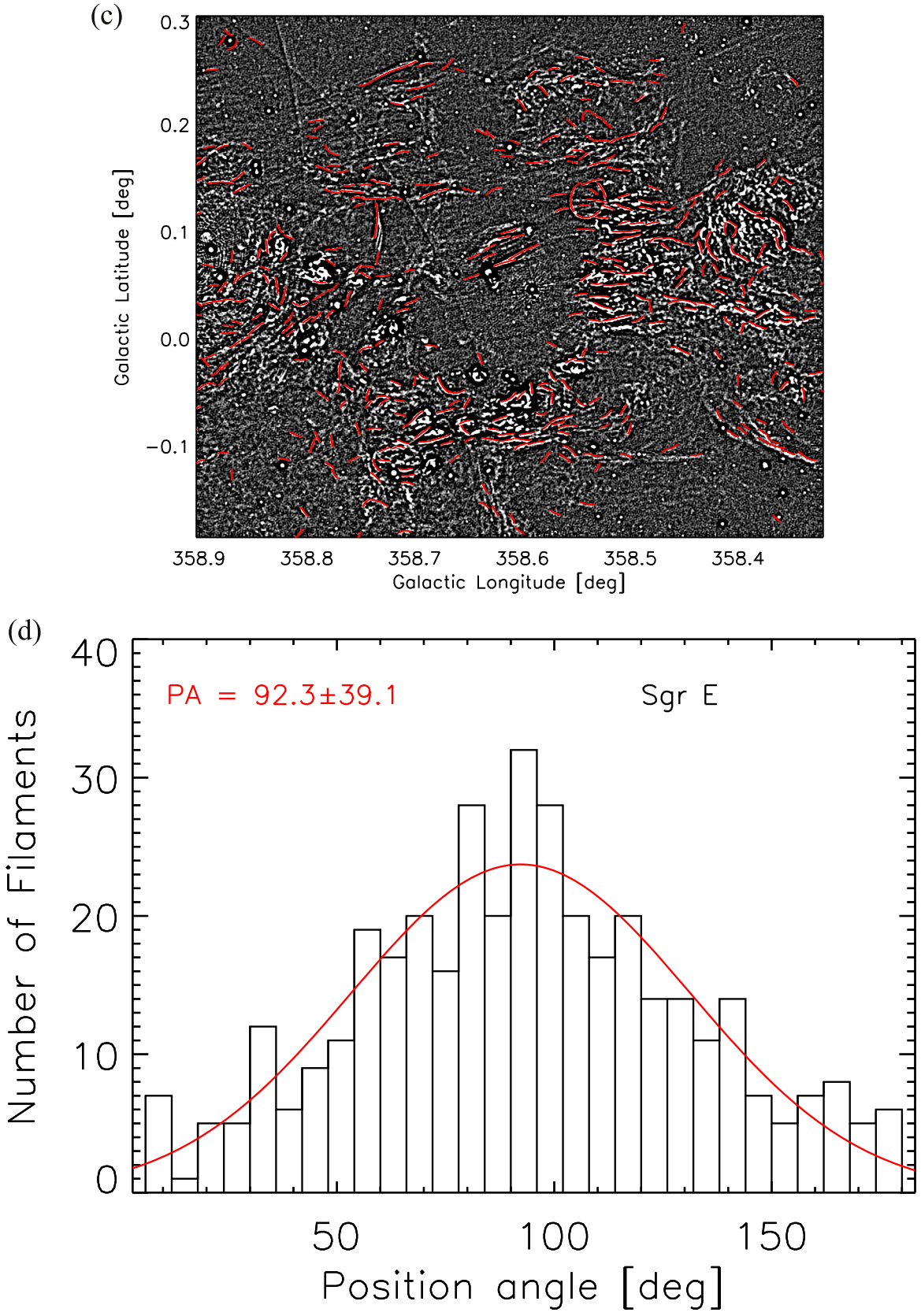

Figure 7. (Continued.)

4. Discussion

Our analysis of the GC filaments' PA distribution indicate two different filament populations. The PAs of the long and short filaments tend to lie in the directions perpendicular and parallel to the Galactic plane, respectively. The vertical and horizontal filaments are characterized to have nonthermal and

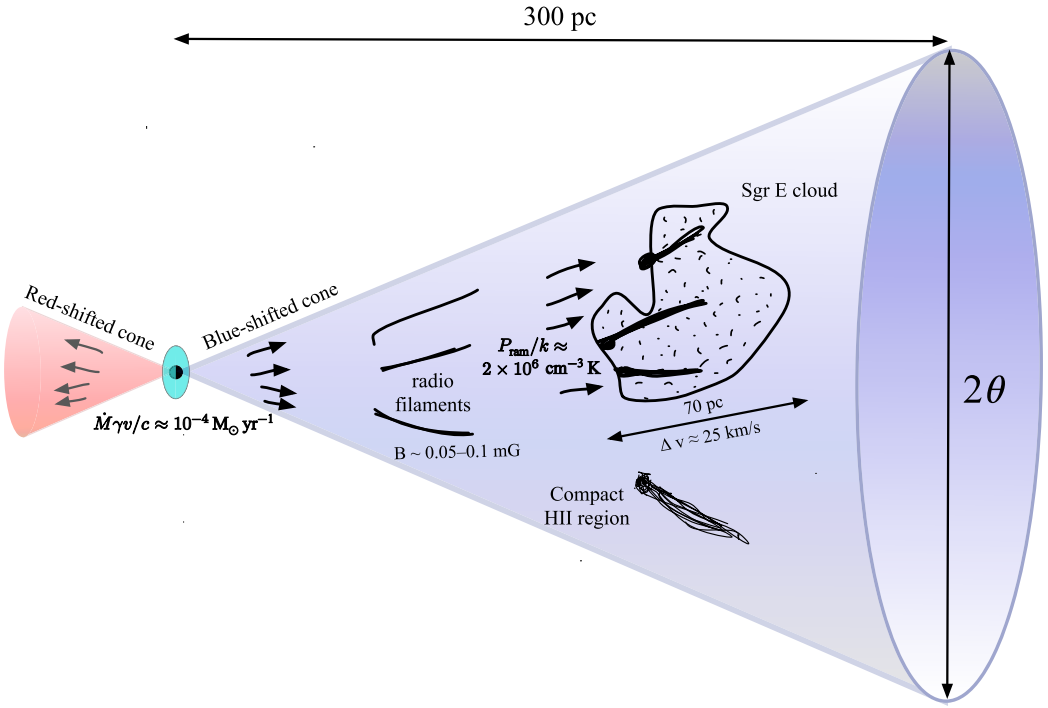

Figure 8. A schematic diagram of a jet-driven outflow with an opening angle 2θ along the Galactic plane.

thermal properties (Yusef-Zadeh et al. 2022a), respectively, based on their spectral indices. While there is clearly an overlap in their properties (e.g., PA, spectral index) a key question is the origin of the bimodal PA distribution of GC filaments.

4.1. Vertical Population of Galactic Center Filaments PA

One population of filaments has orientations that are vertical to within $\sim \pm 25^\circ$ of the Galactic north. The negative and positive PAs tend to be found in positive and negative Galactic longitudes, respectively. There is a slightly reduced number of filaments at PAs $\sim 0^\circ$, giving roughly a bimodal distribution in the histogram. We also note that vertical filaments dominated by long filaments $L > 66''$ have nonthermal spectra. Considering global distribution of vertical filament PAs, there is no evidence that the extension of all filaments PA converge toward Sgr A* or any other compact sources. This suggests that the creation of roughly symmetric PA distribution is in the Galactic plane within a degree of Sgr A*. This is consistent with a trend noticed in the spectral index of nonthermal filaments as they become steeper with increasing absolute Galactic latitude (Yusef-Zadeh et al. 2022a). If synchrotron aging is responsible for the steepening of the spectrum, it implies that the vertical filaments are powered in the Galactic plane (Yusef-Zadeh et al. 2022a).

A scenario for the creation of nonthermal radio filaments uses the high cosmic-ray pressure in the GC estimated from H_3^+ measurements (e.g., Geballe et al. 1999; Oka et al. 2005; Oka & Geballe 2020). This extreme pressure drives a large-scale wind away from the Galactic plane, creating bipolar X-ray and radio emission (Heywood et al. 2019; Ponti et al. 2019; Yusef-Zadeh & Wardle 2019). The nonthermal radio filaments result from the interaction of the large-scale wind and obstacles embedded within the flow, creating the filaments by wrapping the wind's magnetic field around the obstacles (Yusef-Zadeh & Wardle 2019). However, there are alternate models explaining the origin of the vertical filaments (see Yusef-Zadeh et al. 2022a; Sofue 2023 and references therein). This begs the question of the origin of the high cosmic-ray pressure, which is usually attributed to the explosive event a few million years ago that created Fermi bubbles and the bipolar X-ray and radio emission (Heywood et al. 2019; Ponti et al. 2019; Yusef-Zadeh & Wardle 2019).

4.2. Radial Population of Filaments PA in the Galactic Plane

The most interesting result of our study is the discovery of a new population of short filaments' PA that is found along the Galactic plane only at $l < 0^\circ$. There is statistical evidence that short filaments PA point toward Sgr A* with the cone in which the filaments are found has FWHM $\sim 20^\circ$, but the deviations of filament directions from radial is much broader, over a large scale of $\sim$300 pc from Sgr A* at $l < 0^\circ$. This large-scale anisotropy in the filaments PA is interpreted in the context of a large-scale collimated outflow from Sgr A* along the plane. A wind- or jet-driven outflow from Sgr A* has been suggested to explain evidence for outflow in the plane of the Galaxy within a few arcminutes of Sgr A*.

There are eight different spectroscopic, polarimetric, and broadband continuum measurements over a wide range of angular scales extending from $\sim$0.02 to $\sim$25 pc from Sgr A* that have inferred a jet-driven outflow along the Galactic plane (see Yusef-Zadeh et al. 2012, 2020 and references therein). In this picture the jet emerges perpendicular to the equatorial plane of the accretion flow and is aligned roughly east−west in Galactic coordinates. A schematic diagram in Figure 8 showing the interaction of the outflow from Sgr A* with filaments of ionized and molecular gas being aligned roughly along the Galactic flow. For example, blue- and redshifted features in radio recombination line observations on a scale within $14''$ (0.56 pc) of Sgr A* invoke an interpretation in terms of the interaction of a collimated outflow driven outflow from Sgr A*

along $\sim \pm 30^{\circ}$ of the Galactic plane (Royster et al. 2019). In this picture, the blueshifted arm of the jet emerges to the west of Sgr A* making an angle $\sim 45^{\circ}$ to the line of sight.

This small-scale geometry of the jet is consistent with our analysis of filaments PA if the two opposing cones of outflowing material are extrapolated to a scale of $\sim$300 pc. Thus, the blueshifted component of the jet projected along negative longitudes and is tilted toward us with respect to the line of sight, whereas the redshifted component is tilted away from the line of sight projected toward the positive longitudes. However, there is a lack of strong radial filament PAs at positive longitudes in the direction away from the line of sight. This could be explained by confusion due to crowding of radio continuum features in the inner Galaxy.

The jet picture quantified below can also be applied to molecular filaments running parallel to the Galactic plane in Sgr E (Wallace et al. 2022; see Figure 8). An alternative suggestion that has been put forth is that stretching of molecular gas in Sgr E is due to its motion along $x1$ orbits. The Sgr E complex lies at the intersection of CMZ and the Galactic dust lane, so it is possible that the gravitational potential of the bar is responsible for stretching the Sgr E cloud into filaments (Wallace et al. 2022). This suggestion is based on limited ALMA observations over a small region showing CO filaments on a length scale of 2 pc. It is not clear if this suggestion can explain the radial distribution of filament PAs pointing toward Sgr A* on a scale of 300 pc.

4.3. A Model of an Outflow from Sgr A* Along the Galactic Plane

We consider a model in which Sgr A* is the source of an outflow that has sufficient ram pressure to distort and stretch thermal and nonthermal materials that are embedded within the outflow. In this picture, the outflow has a mass-loss rate $\dot{M}$, velocity u, and Lorentz factor γ and is assumed to be directed into opposing cones, each with half-opening angle θ (see Figure 8 for a schematic diagram). The outflow delivers momentum at rate $\dot{p} = \dot{M}\gamma u$ into solid angle $\Omega = 8\pi \sin^2(\theta/2)$. The ram pressure within an outflow cone at distance d from Sgr A* is $P_{\rm ram} = \dot{p}/(\Omega d^2)$, i.e.,

$$P_{\rm ram} = \frac{\dot{M}\gamma u}{8\pi d^2 \sin^2(\theta/2)}. \quad (1)$$

Adopting nominal values $\dot{M}\gamma u/c = 10^{-4}\ M_{\odot}\ {\rm yr}^{-1}$ and $\theta = 20^{\circ}$, consistent with outflow parameters invoked on smaller scales (Yusef-Zadeh et al. 2012; Royster et al. 2019; Yusef-Zadeh et al. 2020), we find that the ram pressure within the cones is $P_{\rm ram}/k = 2 \times 10^6\ {\rm cm}^{-3}$ K at $d = 300$ pc. In order for the outflow to align nonthermal radio filaments with the outflow direction, the ram pressure must exceed the internal filament pressure. Assuming that the magnetic field $B \sim 86\ \mu$ G, the mass outflow rate has to exceed $10^{-4}\ M_{\odot}\ {\rm yr}^{-1}$.

There are also ionized and molecular clouds, such as the Sgr E complex, which are embedded within the outflow. To estimate the velocity gradient that this outflow might induce in an embedded or partially embedded cloud, we note that cloud material with surface density Σ experiences acceleration $a = P_{\rm ram}/\Sigma$. From a standing start, the velocity acquired after being accelerated through distance L is $(2aL)^{1/2}$. Clouds typically exhibit order-unity surface density variations, so the difference in the ram-pressure induced velocity across the cloud is of order v, and we write $\Delta v \approx (2aL)^{1/2}$ (see Figure 8).

We now apply this scenario to the Sgr A E cloud, which exhibits $\Delta v \approx 20$ km s^{-1} over a scale of $0.^{\circ}5$ (Anderson et al. 2020; see their Figure 10), i.e., $L \approx 70$ pc at 8 kpc. We use the outflow parameters adopted above, $10^{-4}\ M_{\odot}\ {\rm yr}^{-1}$. The mean integrated ^{13}CO 2-1 line intensity is 17 K km s^{-1}(Anderson et al. 2020), and using $X_{\rm CO} = 10^{21}\ {\rm cm}^{-2}\ ({\rm K\ km\ s}^{-1})^{-1}$ (Schuller et al. 2017), we obtain a hydrogen column $N_{\rm H} = 1.7 \times 10^{22}{\rm cm}^{-2}$ and compute the cloud's surface density using $\Sigma = 1.4 m_{\rm H} N_{\rm H}$. Then we find that the acceleration $a \approx 4\ {\rm pc\ Myr}^{-2}$, yielding $\Delta v \approx 23$ km s^{-1}, consistent with the observed velocity gradient. The timescale needed to accelerate the material in this scenario is $(2L/a)^{1/2} \approx 6$ Myr, placing a lower limit on the age of the outflow.

One advantage of this model is that the large-scale jet-driven outflow is consistent with a picture that has independently suggested to explain multiple observations at small scales from $\sim$0.5 to 25 pc from Sgr A* where a relativistic jet had previously been proposed (see Yusef-Zadeh et al. 2012; Royster et al. 2019; Yusef-Zadeh et al. 2020 and references therein).

5. Conclusion

In summary, we have presented an analysis of the PA distribution of the entire system of thermal and nonthermal radio filaments in the GC. We use filtered MeerKAT images to determine the PA distributions of the population of nonthermal and thermal radio filaments. We noted alignment of filament directions within 20° of the Galactic plane that suggested a scenario in which a collimated outflow is driven from Sgr A* in the direction along the Galactic plane. The inferred jet is estimated to have a a mass flow rate of $10^{-4}\ M_{\odot}\ {\rm yr}^{-1}$ in order to align nonthermal radio filaments and accelerate thermal gas along the Galactic plane. This outflow emerges perpendicular to the equatorial plane of the accretion flow of Sgr A* and runs along the Galactic plane. The opening angle of the outflow is estimated to be $\sim 40^{\circ}$ with respect to the Galactic plane where the relativistic jet lies, and the age of the outflow is at least 6 Myr.

Work by R.G.A. was supported by NASA under award number 80GSFC21M0002. The MeerKAT telescope is operated by the South African Radio Astronomy Observatory, which is a facility of the National Research Foundation, an agency of the Department of Science and Innovation.

ORCID iDs

R. G. Arendt https://orcid.org/0000-0001-8403-8548
M. Wardle https://orcid.org/0000-0002-1737-0871
I. Heywood https://orcid.org/0000-0001-6864-5057

References

Anderson, L. D., Sormani, M. C., Ginsburg, A., et al. 2020, ApJ, 901, 51
Arendt, R. G., Staguhn, J., Dwek, E., et al. 2019, ApJ, 885, 71
Aschwanden, M. J. 2010, SoPh, 262, 399
Bally, J., & Yusef-Zadeh, F. 1989, ApJ, 336, 173
Condon, J. J., Cotton, W. D., White, S. V., et al. 2021, ApJ, 917, 18
Cram, L. E., Claussen, M. J., Beasley, A. J., Gray, A. D., & Goss, W. M. 1996, MNRAS, 280, 1110
Geballe, T. R., McCall, B. J., Hinkle, K. H., & Oka, T. 1999, ApJ, 510, 251
Gray, A. D. 1994, MNRAS, 270, 822

Gray, A. D., Cram, L. E., Ekers, R. D., & Goss, W. M. 1991, Natur, 353, 237
Gray, A. D., Whiteoak, J. B. Z., Cram, L. E., & Goss, W. M. 1993, MNRAS, 264, 678
Heywood, I., Camilo, F., Cotton, W. D., et al. 2019, Natur, 573, 235
Heywood, I., Rammala, I., Camilo, F., et al. 2022, ApJ, 925, 165
Lang, C. C., Anantharamaiah, K. R., Kassim, N. E., & Lazio, T. J. W. 1999, ApJL, 521, L41
LaRosa, T. N., Brogan, C. L., & Shore, S. N. 2005, ApJL, 626, L23
Law, C. J., Yusef-Zadeh, F., & Cotton, W. D. 2008, ApJS, 177, 515
Law, C. J., Yusef-Zadeh, F., Cotton, W. D., & Maddalena, R. J. 2008b, ApJS, 177, 255
Liszt, H. S. 1985, ApJ, 293, L65
Lu, F. J., Wang, Q. D., & Lang, C. C. 2003, AJ, 126, 319
Nord, M. E., Lazio, T. J. W., & Kassim, N. E. 2004, AJ, 128, 1646
Oka, T., & Geballe, T. R. 2020, ApJ, 902, 9
Oka, T., Geballe, T. R., Goto, M., Usuda, T., & McCall, B. J. 2005, ApJ, 632, 882
Ponti, G., Hofmann, F., Churazov, E., et al. 2019, Natur, 567, 347
Pound, M. W., & Yusef-Zadeh, F. 2018, MNRAS, 473, 2899
Ramatsoku, M., Murgia, M., Vacca, V., et al. 2020, A&A, 636, L1
Reich, W., Sofue, Y., & Matsuo, H. 2000, PASJ, 52, 355
Royster, M. J., Yusef-Zadeh, F., & Wardle, M. 2019, ApJ, 872, 2
Rudnick, L., Brüggen, M., Brunetti, G., et al. 2022, ApJ, 935, 168
Sakano, M., Warwick, R. S., Decourchelle, A., & Predehl, P. 2003, MNRAS, 340, 747
Schuller, F., Csengeri, T., Urquhart, J. S., et al. 2017, A&A, 601, A124
Shimwell, T. W., Luckin, J., Brüggen, M., et al. 2016, MNRAS, 459, 277
Sofue, Y. 2023, MNRAS, 518, 6273
Sofue, Y., Murata, Y., & Reich, W. 1992, PASJ, 44, 367
Staguhn, J., Arendt, R. G., Dwek, E., et al. 2019, ApJ, 885, 72
Wallace, J., Battersby, C., Mills, E. A. C., et al. 2022, ApJ, 939, 58
Yusef-Zadeh, F. 2012, ApJL, 759, L11
Yusef-Zadeh, F., Arendt, R., Bushouse, H., et al. 2012, ApJL, 758, L11
Yusef-Zadeh, F., Arendt, R. G., & Wardle, M. 2022a, ApJL, 925, L18
Yusef-Zadeh, F., Arendt, R. G., Wardle, M., et al. 2022b, MNRAS, 515, 3059
Yusef-Zadeh, F., Arendt, R. G., & Wardle, M. 2022d, ApJL, 939, L21
Yusef-Zadeh, F., Arendt, R. G., Wardle, M., Heywood, I., & Cotton, W. 2022c, MNRAS, 517, 294
Yusef-Zadeh, F., Hewitt, J. W., & Cotton, W. 2004, ApJS, 155, 421
Yusef-Zadeh, F., Morris, M., & Chance, D. 1984, Natur, 310, 557
Yusef-Zadeh, F., Royster, M., & Wardle, M. 2020, MNRAS, 499, 3909
Yusef-Zadeh, F., & Wardle, M. 2019, MNRAS, 490, L1
Yusef-Zadeh, F., Wardle, M., Heinke, C., et al. 2021, MNRAS, 500, 3142
Yusef-Zadeh, F., Wardle, M., Muno, M., Law, C., & Pound, M. 2005, AdSpR, 35, 1074
Zhang, S., Hailey, C. J., Baganoff, F. K., et al. 2014, ApJ, 784, 6
Zhang, S., Zhu, Z., Li, H., et al. 2020, ApJ, 893, 3